SciEn

Proceedings of 8th International Conference on Mechanical Engineering and Renewable Energy 2025
10-12 December, 2025, Chattogram, BANGLADESH

SciEn Conference Series: Engineering Vol. 4, 2026, pp 111-116 https://doi.org/10.38032/scse.2026.4.59

Gesture Based Rover for Rapid Disaster Response

Md. Nafis Mahmud, Arnob Roy, Samiul Kabir Rohan, Zibon Nesa Zim*

Department of Mechatronics Engineering, Khulna University of Engineering & Technology, Khulna-9203, Bangladesh.

ABSTRACT

Post disaster search and rescue missions pose significant challenges to modern robotics, highlighting the need for further innovation. These hazardous, unstructured and unpredictable environments require solutions that are reliable, fast and easy to deploy. This paper introduces the prototype development and performance evaluation of a compact, low-cost unmanned rover system engineered to assist in such operations by providing real-time environmental feedback and visual monitoring. The rover features hand gesture-based control and omnidirectional movement that enable natural and efficient remote maneuvering in constrained spaces. Additional features such as transmitting continuous video and thermal feed to a remote station and sharing live location data enhances situational awareness and rapid decision making. Its design emphasizes agility, obstacle-negotiation capability, and support functions, ensuring reliable performance in remote unstable areas. By combining affordability with an operator-friendly interface, the rover offers a scalable and practical tool for field responses in time-critical missions.

Keywords: Unmanned rover, Hand gesture control, Omnidirectional movement, Disaster response and Live video feed.

1. Introduction

Natural disasters are an inevitable part of the world, striking unexpectedly and causing widespread damage. However, numerous disasters also result from political unrest or human negligence, resulting in loss of life, disappearances and widespread injuries. Some notable examples are as follows:

- On March 26, 2023, a devastating landslide occurred in Alausí, Ecuador, triggered by intense and prolonged rainfall combined with unstable volcanic soils and steep terrain[1]. The disaster resulted in over 23 deaths, approximately 38 injuries, and around 67 people missing, along with significant destruction of homes and infrastructure [2]. Contributing factors included natural geological conditions as well as human activities such as deforestation and unplanned construction.
- The Rana Plaza collapsed on April 24, 2013, when an eight-story commercial building in Bangladesh collapsed due to structural failure. The disaster resulted in the deaths of 1,134 people [3] and injuries of approximately 2,500, making it one of the deadliest structural failures in Bangladesh's history. The rescue efforts, which lasted 19 days, were mainly carried out through the manual efforts of volunteers, the general public, police, fire services, and military personnel [4].

In addition to the incidents described above, numerous other catastrophic events have resulted in hundreds of people going missing and never being found. Historically, when technological capabilities were limited, search and rescue operations relied entirely on manual efforts, which were both time-consuming and hazardous. Advances in technology have since provided new approaches for addressing such challenges. In many cases, humans cannot directly access complex or hazardous locations, or may arrive too late to effect timely rescue. In these situations, the use of robots, drones and modern sensor-based equipment can make rescue operations more efficient, faster and safer. Consequently, technology has become an indispensable component in contemporary disaster response. The following section highlights recent incidents where modern technologies, including search and rescue robots, drones and thermal imaging systems, have been employed to locate missing persons and assist in survivor rescue.

- On March 11, 2011, a magnitude 9.0 earthquake, followed by a tsunami, struck Japan, resulting in nuclear meltdowns at three reactors of the Fukushima Daiichi Nuclear Power Plant. The high radiation levels around the reactors made manual search and rescue operations hazardous. Consequently, radiation-tolerant robots were deployed to perform inspections, data collection and decontamination operations. Robots deployed included PackBot (iRobot, USA) and Quince (Japan) [5].
- On April 25, 2015, a magnitude 7.8 earthquake struck Nepal. The DJI Phantom (China) and SenseFly eBee drones were deployed to support rapid rescue and relief operations in remote mountainous regions. These drones facilitated the detection of debris and survivors. The Humanitarian UAV Network (UAViators) and other NGOs participated in these drone missions, enhancing the effectiveness of rescue operations [6].

Advances in technology have significantly enhanced the capabilities of robots and drones used in rescue operations. Unlike earlier observation robots or drones, modern systems are not only capable of monitoring environments but can also explore confined and hazardous areas, detect gases or heat, transport injured individuals and identify hazardous substances. Some examples are as follows:

- Robear, developed by RIKEN, is specifically designed to lift and safely transport the injured [7].

*Corresponding Author Email Address: nafis.mahmud222@gmail.com

- Elios 3, developed by Flyability, is able to fly in congested and dangerous spaces to can find gas leaks or cracks.
- Fotokite Sigma is a tethered drone providing continuous video and data to fire departments or rescue organizations.

Existing robotic systems exhibit several limitations, including limited mobility; short battery life; communication challenges; suboptimal sensor performance; lack of adaptability; restricted operational range; high cost; and complex control mechanisms.

Here, we propose an innovative rover with solutions to all these problems. In this paper, we present an unmanned ground rover for risky search and survey operations. It incorporates easy hand gesture control using an MPU6050 sensor and Kalman filter and can be remotely controlled by the rover via the low-latency ESP-NOW protocol.

The rover's omnidirectional wheel drive facilitates easy movement. Live video streaming, thermal imaging, real-time location sharing, and onboard voltage monitoring are special features.

The system is a low-cost, ready-to-use system for rescue missions.

2. Methodology

This section covers the overall technical components, design parameters and functional features of the rover. The working principle of this Robot is described in the following paragraphs.

2.1 Design Parameters

2.1.1 Extended Wheelbase:

To enable the rover to traverse small gaps and climb sharply angled or steep surfaces with ease, the wheels are positioned slightly forward and outward relative to the main body. This configuration allows the rover to navigate inclined and uneven terrains while enhancing its overall stability.

2.1.2 Ground Clearance:

To enable traversal over small rubble and debris-laden areas, the motors are mounted beneath the main rover body, providing sufficient ground clearance. This design allows the rover to move smoothly over obstacles and uneven terrain without becoming immobilized, which is critical during search and rescue missions.

2.1.3 Length to Width Ratio:

The rover's body is intentionally designed to be longer than it is wide. This configuration facilitates easier turning and rotation, as smaller motor inputs are required to achieve significant angular displacement, resulting in more responsive control in cluttered environments.

2.1.4 Battery Placement:

The weight distribution and center of gravity play a critical role in the rover's overall mobility. The batteries, which constitute the majority of the rover's weight, are positioned near the center and lower portion of the chassis to maintain a low center of gravity. This arrangement enhances stability and reduces the risk of tipping on uneven terrain.

2.2 Gesture Recognition and Transmission

2.2.1 Sensing:

The gesture recognition system is mainly driven by the MPU6050 sensor, which combines a 3-axis accelerometer and a 3-axis gyroscope in a compact module. It has the ability to capture both linear acceleration and angular velocity, that can be combined to precisely detect hand movement in 3-D space along X, Y and Z axis. The sensor also features a 16-bit ADC (Analog to Digital Converter) for each channel and offers a sensitivity range of ±2g to ±16g for acceleration and ±250°/s to ±2000°/s for rotation. It communicates with the micro-controller via I2C protocol. To track the user's hand orientation in real time, the MPU6050 was mounted directly on a hand glove.

2.2.2 Kalman Filter:

The Kalman Filter is a mathematical algorithm that provides an effective recurrent solution to the problem estimating the state of a dynamic system from noisy measurement. It obtains an estimate of the state value through an iterative calculation. And it is the best estimate for linear systems with Gaussian white noise [8]. To achieve precise gesture recognition, accurate estimation of roll and pitch angles is needed from the raw data of MPU6050. However, both accelerometer and gyroscope have their own limitations. Accelerometer's data is sensitive to vibrations and sudden motion. Gyroscope's data has a tendency to drift over time. To overcome this problem, a 2-D Kalman filter was implemented. The steps of angle estimation are mentioned below:

1) *Raw Angle Calculation from Accelerometer:* The raw roll (θ) and pitch (ϕ) angles can be estimated from the acceleration values as:

$$Roll\ (\theta) = \arctan\left(\frac{a_y}{\sqrt{a_x^2+a_z^2}}\right)\times\frac{180}{\pi} \quad (1)$$

$$Pitch\ (\phi) = \arctan\left(\frac{-a_x}{\sqrt{a_y^2+a_z^2}}\right)\times\frac{180}{\pi} \quad (2)$$

Where a_x, a_y, a_z are acceleration in X, Y and Z axes respectively.

2) *Raw Angle Calculation from Gyroscope:* The gyroscope gives angular velocity as output. To get orientation,

$$\theta_{gyro} = \theta_{prev} + \omega_x \cdot \Delta t \quad (3)$$

$$\phi_{gyro} = \phi_{prev} + \omega_y \cdot \Delta t \quad (4)$$

Where ω_x, ω_y are rotational velocities around X and Y axes.

3) *Kalman Filter Implementation:* The state-space model for the Kalman Filter can be simply denoted as follows:

Prediction step:

$$\hat{x}_{k|k-1} = F\hat{x}_{k-1|k-1} + Bu_k \quad (5)$$

$$P_{k|k-1} = FP_{k-1|k-1}\ F^T + Q \quad (6)$$

Update step:

$$K_k = \frac{P_{k|k-1}H_k^{\ T}}{H_t P_{t|t-1} H_t^{\ T} + R} \quad (7)$$

$$\hat{x}_{k|k} = \hat{x}_{k|k-1} + K_k(y_k - H_k\hat{x}_{k|k-1}) \quad (8)$$

$$P_{k|k} = (I - K_k H_k)P_{k|k-1} \quad (9)$$

Where $\hat{x}$ is the state estimate, P is a state error covariance matrix, Q is a process noise covariance matrix, R is a measurement noise covariance matrix, H is a measurement matrix, y_k is a measurement variable, T is the transpose matrix, K_k is Kalman filter gain and I is identity matrix, F is a state transition matrix [9].

4) *System design:* The design of this system requires some key components. The system block diagram in shown in Fig. 1.

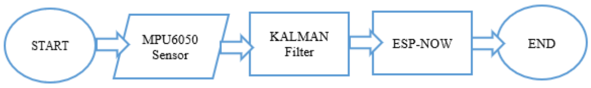

Fig.1: Block diagram of Kalman Filter

The actual filter parameters used in the module are:

Sampling rate, T_s = 0.004 s (or 250 Hz)
Measurement Noise Covariance, R = 9
Process Noise Covariance, Q = 0.000256

5) *Analysis of Static Filtering*: The before and after results of applying static Kalman filter can be seen in Fig. 2.

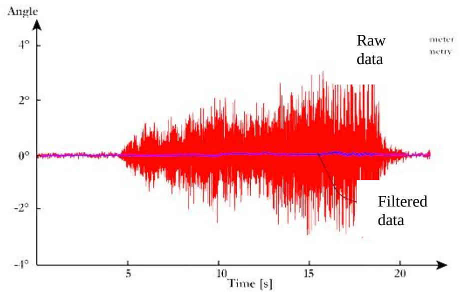

Fig.2: Filtration example of static Kalman Filter

By applying this filter, we were able to reduce noise and achieve a drift-free orientation angle of hand movement.

2.2.3 Push Button:

A tactile push button is added for turning the headlights on the rover on or off. It operates using a simple active-low logic. The pressed signal is transmitted via the ESP-NOW protocol to the receiver module, which switches the headlights on or off accordingly.

2.2.4 Transmitter Module:

The transmitter module is the heart of the gesture control interface. This acts as a bridge between human motion machine response. The module consists of the MPU6050 sensor, tactile push button, ESP32 microcontroller, Li-ion battery, Boost module and on/off switch. The circuit diagram is shown in Fig. 3. The whole transmitter module is housed in the glove (Fig. 8a) which the user wears to control the rover.

2.2.5 Control Signs:

The particular gestures or the hand signs that are used to control the rover and their corresponding commands are listed in Table 1 [10]. To compensate for human errors, a 30˚ margin has been kept under “Still command.”

2.3 Communication Protocol

2.3.1 ESP-NOW:

The ESP-NOW is a wireless communication protocol developed by Espressif exclusively for ESP32 microcontrollers [11]. It enables direct peer-to-peer (P2P) data transmission without the need for an access point [12]. In our system, the ESP32 on the glove acts as the transmitter that sends gesture data packets including roll, pitch and button state. And the ESP32 on the rover is used as the receiver that interprets the incoming data and send commands for the motor drivers.

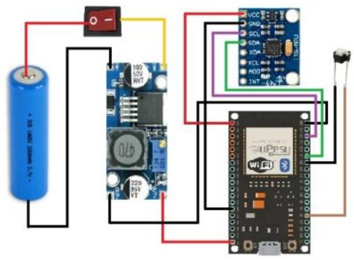

Fig.3: Wiring diagram of the controller

Table 1: Hand Gesture Control Signs

Hand Gesture	Turn Angle Range	Command	Speed Constant
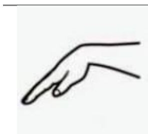	30˚-70˚	Front	4
	70˚-90˚	Extreme Front	10
	30˚-70˚	Back	4
	70˚-90˚	Extreme Back	10
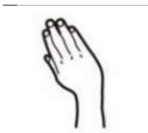	30˚-70˚	Left	4
	70˚-90˚	Extreme Left	10
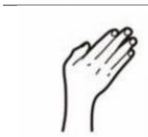	30˚-70˚	Right	4
	70˚-90˚	Extreme Right	10
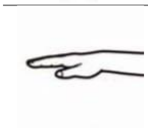	0˚-30˚	Still	0

2.3.2 ESP32-CAM:

The ESP32-CAM module combines the computing power of the ESP32-S chip with an onboard OV2640 camera which is capable of capturing VGA and up to 1600x1200 UXGA resolution images. It supports Wi-Fi 802.11 b/g/n, allowing it to connect either to a local hotspot or create its own access point for direct peer-to-peer communication. In our implementation, it is configured in station mode, streaming to any connected device on the same network through an IP address (e.g., 192.168.43.48).

2.3.3 Thermal-CAM:

For aerial thermal imaging, a Melexix MLX90640 sensor was mounted on the rover. This is a non-contact 2D thermal imaging array sensor that can detect heat signatures in areas with low visibility. It has a resolution of 32×24 pixels and has a temperature measurement range of −40°C to +300°C. The video feed from the sensor is streamed alongside ESP32-CAM via Wi-Fi through local IP address.

2.4 Drive Mechanism

2.4.1 Motors:

The motors are the main driving component of the rover's mobility system. In this system, four TT DC gear motors are used. Each motor has a rated speed of 150 RPM at 12V with a stall torque of 0.35 kg·cm.

2.4.2 Motor Drivers:

The motors of the rover are driven by two L298N dual H-bridge motor drivers, which can efficiently handle the direction and PWM speed control. These drivers in particular, can support motor supply voltages from 5V to 35V and delivers continuous current up to 2A per channel.

2.4.3 Wheels:

To achieve proper omnidirectional motion, four mecanum wheels are used. Mecanum wheel is a specialized type of wheel which is designed for omnidirectional movement that allows the robot to move in any direction without changing their orientation. The advantage of the omnidirectional robot is that it can move independently as well as work in three degrees of freedom. Although it can increase its movability in an effective manner [13]. It consists of a set of rolls placed symmetrically around the wheel. Usually, it has an angle δ between the roller to the axis of the wheel hub is ±45◦ [14]. It can be seen from the Fig. 4. [15]. The kinematics of mecanum wheels are as follows:

Fig. 4 shows the configuration of a robot with four omnidirectional wheels [16]. Inverse kinematic model of the mobile robot is derived from the movement vector of four-wheel drive robot platform [17].

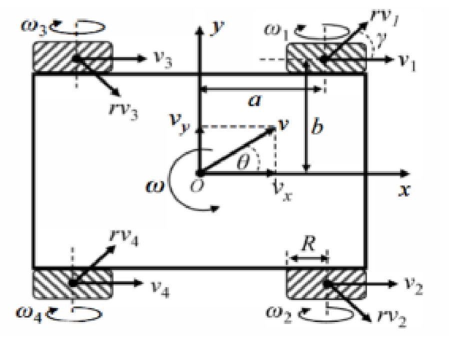

Fig.4: Kinematic diagram of mecanum wheel

Vector of the robot velocity v which has parallel direction to the x coordinate of V_x and V_y vector components are derived by,

$$V_x = v \cos \theta \qquad (10)$$
$$V_y = v \sin \theta \qquad (11)$$

Where θ is the lateral direction angle of robot movement velocity. Angular velocity of the robot is defined by ω at the center point of the robot that indicates yaw movement. Robot dimension is denoted by radius of a and b between body center robot and wheel axis of a_i: $\{a, a, -a, -a\}$ and b_i: $\{b, -b, b, -b\}$ where i: $\{1, 2, 3, 4\}$ which represented wheel numbers. Linear velocity vector of the wheel and velocity of mecanum roller direction of each wheel are indicated by V_i and rV_i, respectively. Tilted angle γ between v and rv is 45° which represents the mecanum roller angle each wheel of γ_i: $\{\pi/4, -\pi/4, -\pi/4, \pi/4\}$. The velocity vector equation of the robot toward coordinate system component can be calculated by,

$$V_i + rV_i \cos(\gamma) = V_x - b_i\, \omega \qquad (12)$$
$$rV_i \sin(\gamma) = V_y + a_i\, \omega \qquad (13)$$

From (12) and (13) the linear velocity for each wheel can be obtained,

$$V_i = V_x - b_i\, \omega - \frac{V_y + a_i\, \omega}{\tan(\gamma_i)} \qquad (14)$$

Since $\tan(\gamma_i)$ in (14) can be denoted by $\tan(\gamma_i)$: $\{1, -1, -1, 1\}$, the linear velocity of the mecanum wheel is:

$$V_1 = V_x - V_y - a\omega - b\omega \qquad (15)$$
$$V_2 = V_x + V_y + a\omega + b\omega \qquad (16)$$
$$V_3 = V_x + V_y - a\omega - b\omega \qquad (17)$$
$$V_4 = V_x - V_y + a\omega + b\omega \qquad (18)$$

While the angular wheel velocities are Vi = ω*R and R is the radius of four mecanum wheels, (15) to (18) can be modified as,

$$\begin{bmatrix} \omega_1 \\ \omega_2 \\ \omega_3 \\ \omega_4 \end{bmatrix} = \frac{1}{R} \begin{bmatrix} 1 & -1 & -(a+b) \\ 1 & 1 & (a+b) \\ 1 & 1 & -(a+b) \\ 1 & -1 & (a+b) \end{bmatrix} \begin{bmatrix} V_x \\ V_y \\ \omega \end{bmatrix} \qquad (19)$$

Equation (19) shows the mathematical model of the inverse kinematics to be implemented to obtain angular velocities of each mecanum wheel by input of vector component of V_x, V_y and ω according to the lateral direction angle θ without changes the robot facing in certain direction [18].

2.4.4 Power Supply:

The rover's power supply system is based on two 18650 Li-ion batteries connected in series, providing an average voltage of 7.4 V and a capacity of 650 mAh each, enabling over 45 minutes of operation on a single charge. To increase the voltage, a DC-DC boost converter is incorporated, stepping up the 7.4 V from the batteries to a stable 12 V output. This ensures that the motors receive sufficient power even as the batteries discharge.

2.4.5 Receiver Module:

This module interprets the incoming data from the transmitter module and translates them into rover's motion. The module consists of an ESP32 microcontroller, batteries, boost converter module, two L298N motor drivers, four DC gear motors, two pairs of mecanum wheels, few 100kΩ resistors and two LEDs. The circuit diagram is shown in Fig. 5. All the components are placed on a PCB prototype board in such a way that all the points discussed in the design parameters section are met (Fig. 8b).

2.4.6 Location Tracking:

To achieve reliable location tracking and zero power consumption from rover's battery, an Apple AirTag is attached under the body of the rover. This method eliminates the need for any dedicated GPS module that can be costly or hard to calibrate. Using the Find My Device app on an iPhone, the location of the rover can be traced.

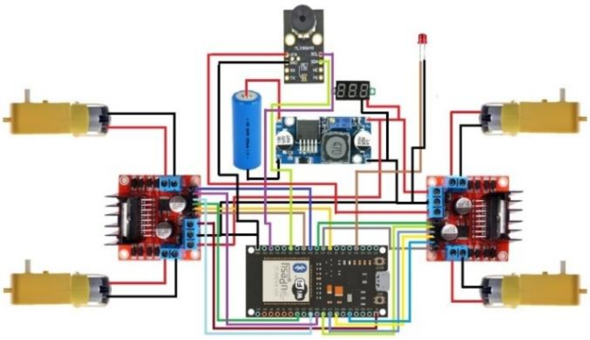

Fig.5: *Wiring diagram of the rover*

2.5 Live Video Feed

2.5.1 Transmitter-end:

To get live video feed from the ESP-CAM, the module was connected to the local network. The SSID and password is added to the code. Then the local IP address of the module was found by connecting it with the computer (Fig. 6) which could be accessed.

Fig.6: Video transmission from sender

2.5.2 Receiver-end:

After accessing the IP address on our browser, the following page (Fig. 7) was displayed, which allows us to adjust the frame and effects. The feed from the thermal sensor can also be viewed in the same way.

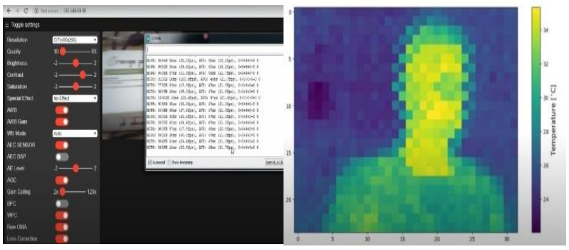

Fig.7: Video transmission to receiver

3. Cost Analysis

One of the key components of the development of this rover was affordability without compromising on functionality. The breakdown of the approximate costs for each component of the rover is listed in Table 2.

4. Test Results and Discussion

We have conducted several tests to analyze the performance of the rover in real disaster response cases. Below are the results of these tests.

4.1 Range Test:

Our ESP-NOW test showed ms-level latency and supported peer-to-peer links without a router. In open-field trials, stability remained above 99 % up to 150 m, and field demonstrations have pushed ranges to 220 m, even 400 m in ideal conditions.

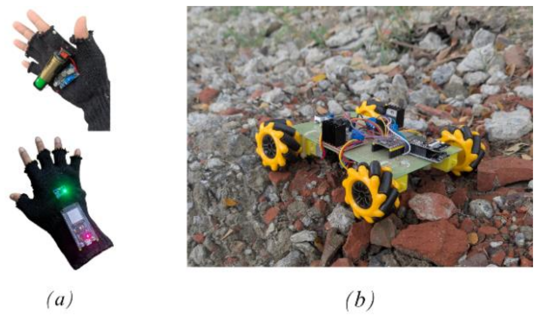

Fig.8: Rover and controller prototype (a) Controller (b) Rover moving on debris

Table 2: Cost Analysis

Component	Unit Price (BDT)	Quantity	Total (BDT)
ESP32 (with Wi-Fi and BT)	450	2	900
MPU6050	150	1	150
MLX90640	5,800	1	5,800
ESP32-CAM Module	650	1	650
L298N Motor Driver	150	2	300
Motors	120	4	480
Mecanum Wheels	475	4	1,900
Batteries	60	3	180
DC Boost Module	55	2	110
Chassis Materials (Board, Screws, Nuts)	200	1	200
Apple AirTag	2,200	1	2,200
Push Buttons and Switches	20	3	60
LED	5	2	10
Connecting Wire	100	-	100
	Total Estimated Cost		**13,040**

4.2 Connectivity Test:

Here we simulated real-world environmental obstructions by introducing walls, metal barriers and wooden panels between the rover and the receiver. The idea was to check how the signal behaves when passing through various materials. We found that:

- Wooden doors and glass panels reduced signal strength slightly but didn't disrupt communication.
- Concrete walls introduced notable signal degradation; communication became unstable after crossing two solid concrete barriers.
- Metal surfaces like cabinets and fences caused signal reflections and partial data corruption.

4.3 Climb Test:

We conducted a climb test by gradually increasing the angle of an inclined ramp made of wood and later, rough concrete. The rover successfully climbed inclines up to 25 degrees without slippage or motor stall. At 30 degrees, the ascent became significantly slower, and beyond 45 degrees, traction loss was observed on smooth surfaces. This test confirms that the rover is capable of handling ramps, debris piles and minor rubbles which makes it suitable for exploration in semi-rough environments like collapsed indoor structures or construction zones.

4.4 Water and Dust Resistance Test:

The rover is not designed to withstand water or radiation exposure and no measures were implemented to prevent dust ingress either. This is a major limitation to our design of the rover.

4.5 Battery Test:

Experimental evaluations demonstrate that the onboard battery system supports approximately 45 minutes of continuous operation per charge; this operational duration can be extended by integrating additional battery modules into the rover.

These tests show that our rover prototype is capable of handling real-life rapid disaster response with some minor upgrades. Specially the connectivity and battery tests demonstrate that our rover outperforms AliOS-3, RoBear and other previously discussed robots, as it effectively addresses the limitations reported in their respective studies. Our rover also incorporates a low-cost, compact, lightweight, and cost-effective design with wireless real-time control, addressing limitations identified in the previously mentioned studies.

5. Conclusion and Future Works

This paper presents a functional, low-cost, and compact ground rover developed for urban search and rescue operations. Emphasizing gesture-based control, real-time sensory feedback and terrain adaptability, the system demonstrates strong potential for deployment in high-risk, debris-filled environments where human access is limited. Overall, the platform serves as a practical solution to minimize human efforts during critical rescue missions, contributing to safer and more efficient response operation.

Some proposals to upgrade the rover are as follows:

- Upgrading sensor and motors.
- Using spring suspensions for the wheels to reduce vibrations.
- Implementing camera-vision for autonomous control.
- Using stronger and more durable build material.
- Using drone for remote access to the disaster site.
- Making a completely water and dust proof rover body.

6. References

[1] L. Pilatasig *et al.*, "Casual-Nuevo Alausí Landslide (Ecuador, March 2023): A Case Study on the Influence of the Anthropogenic Factors," *GeoHazards 2025, Vol. 6, Page 28*, vol. 6, no. 2, p. 28, Jun. 2025.

[2] "Death toll from Ecuador landslide deaths rises to 17, over 70 remain missing | Reuters." Accessed: Oct. 06, 2025. [Online].

[3] H. Tansy, "Reliving the Rana Plaza factory collapse: a history of cities in 50 buildings, day 22," *The Observer*, Apr. 2015, [Online]. Available: https://www.theguardian.com/cities/2015/apr/23/rana-plaza-factory-collapse-history-cities-50-buildings

[4] L. Bossavie, Y. Cho, and R. Heath, "The effects of international scrutiny on manufacturing workers: Evidence from the Rana Plaza collapse in Bangladesh," Journal of Development Economics, vol. 163, no. C, 2023, Art. no. 103107.

[5] K. Gai *et al.*, "You may also like Emergency Response Mechanism and Improvement of Hazardous Chemicals Accidents in Qing Yang City Research Progress of Nuclear Emergency Response Robot."

[6] "3 Days Above the Clouds. Nepal. April, 2015 - DJI." Accessed: Oct. 07, 2025. [Online]. Available: https://www.dji.com/lv/newsroom/news/3-days-above-the-clouds-nepal-april-2015

[7] "The strong robot with the gentle touch | RIKEN." Accessed: Oct. 07, 2025. [Online]. Available: https://www.riken.jp/en/news_pubs/research_news/pr/2015/20150223_2/

[8] R. I. Alfian, A. Ma'Arif, and S. Sunardi, "Noise reduction in the accelerometer and gyroscope sensor with the Kalman filter algorithm," *Journal of Robotics and Control (JRC)*, vol. 2, no. 3, pp. 180–189, May 2021.

[9] S. Bratić, Đ. Prosenica, L. Gajić, S. Terzić, S. Kasapović, and M. Urekar, "Comparing Filter Efficiency: Complementary vs. Kalman Filters on Accelerometer and Gyroscope Signals," in *Proceedings of 11th International Conference IcETRAN 2024*, ETRAN Society, Academic Mind, Belgrade, Jul. 2024, pp. 111–116.

[10] P. Yeap and S. Muraki, "Effect of Wrist Deviation on Median Nerve Cross-Sectional Area at Proximal Carpal Tunnel Level," 2014.

[11] "ESP-NOW Wireless Communication Protocol | Espressif Systems." [Online]. Available: https://www.espressif.com/en/solutions/low-power-solutions/esp-now

[12] "Exploring wireless communication protocols on ESP32 platform for outdoor applications · Developer Portal." [Online]. Available: https://developer.espressif.com/blog/esp-now-for-outdoor-applications/

[13] A. Mogra, S. Verma, N. Dhengre, and A. Gupta, "Design and manufacturing of mecanum wheel for omnidirectional robot."

[14] A. Gfrerrer, "Geometry and kinematics of the Mecanum wheel," *Comput Aided Geom Des*, vol. 25, no. 9, pp. 784–791, Dec. 2008.

[15] T. Sha, "Mecanum wheels robot modeling and path tracking," *Applied and Computational Engineering*, vol. 46, no. 1, pp. 246–253, Mar. 2024.

[16] F. Iotti, A. Ranjan, F. Angelini, and M. Garabini, "OmniQuad: A wheeled-legged hybrid robot with omnidirectional wheels," *Mech Mach Theory*, vol. 214, p. 106125, Oct. 2025.

[17] H. T. Truong, "Adaptive Voltage Control for DC Motors of Omnidirectional Mobile Robot with Prevent Wheel Slippage," IEEE Access, Jan. 2025, Art. no. PP(99):1–1.

[18] E. Maulana, M. A. Muslim, and V. Hendrayawan, "Inverse kinematic implementation of four-wheels mecanum drive mobile robot using stepper motors," in Proceedings of the 2015 International Seminar on Intelligent Technology and Its Applications (ISITIA), May 2015, pp. 51–56.